CHEMICAL PHYSICS

Tracking surface charge dynamics on single nanoparticles

Ritika Dagar[1,2]*†, Wenbin Zhang[1,2,3]*†, Philipp Rosenberger[1,2], Thomas M. Linker[4], Ana Sousa-Castillo[5], Marcel Neuhaus[1,2], Sambit Mitra[1,2], Shubhadeep Biswas[1,2,4], Alexandra Feinberg[4], Adam M. Summers[4], Aiichiro Nakano[6], Priya Vashishta[6], Fuyuki Shimojo[7], Jian Wu[3], Cesar Costa Vera[1,8], Stefan A. Maier[9,10], Emiliano Cortés[5], Boris Bergues[1,2], Matthias F. Kling[1,2,4,11]*

Surface charges play a fundamental role in physics and chemistry, in particular in shaping the catalytic properties of nanomaterials. However, tracking nanoscale surface charge dynamics remains challenging due to the involved length and time scales. Here, we demonstrate time-resolved access to the nanoscale charge dynamics on dielectric nanoparticles using reaction nanoscopy. We present a four-dimensional visualization of the spatiotemporal evolution of the charge density on individual SiO_2 nanoparticles under strong-field irradiation with femtosecond-nanometer resolution. The initially localized surface charges exhibit a biexponential redistribution over time. Our findings reveal the influence of surface charges on surface molecular bonding through quantum dynamical simulations. We performed semi-classical simulations to uncover the roles of diffusion and charge loss in the surface charge redistribution process. Understanding nanoscale surface charge dynamics and its influence on chemical bonding on a single-nanoparticle level unlocks an increased ability to address global needs in renewable energy and advanced health care.

INTRODUCTION

Altering charges in catalysts, surfaces, and even at the atomic level has been pivotal in numerous applications across diverse fields. Surface charges critically affect nanoparticle (NP) functionality in essential domains like photocatalysis (1–3), solar cells (4), and biomedical applications (5, 6). The surface charge density and electrostatic potential of NPs determine their cellular uptake ability and interaction with other biological environments (5). Understanding the dynamics of surface charges holds substantial promise for advancing atomic-scale technologies (7) and enhancing our grasp of electrochemical reactions (8), catalyst selectivity (9), and surface adatom behavior (10). Surface charge manipulation in catalytic systems is an emerging field offering enhanced performance. Engineering surface charge states can endow unique functions upon catalytic nanosystems in terms of reactant adsorption and activation (11). The surface charges on NP surfaces can induce and/or enhance catalytic reactions through mechanisms like surface potential alteration, charge transfer, localized heating, and reactant binding (12, 13). Despite

these advancements, establishing a precise relationship between the dynamics of surface charges and the catalytic efficacy of NPs remains an open challenge, underscoring the need for further investigation.

Despite the importance of charge carriers in modifying photocatalytic reaction pathways, their intriguing ultrafast dynamics have yet to be fully elucidated. Ultrafast processes related to charge carriers include electron scattering (14), nanoplasma expansion (15, 16), charge regulation (17, 18), and charge diffusion (19–27). Unwrapping these processes on their natural timescales is critical for the development of next-generation solar harvesting devices (2). Prior studies characterized surface charge generation and redistribution processes using methods such as atomic force microscopy (24, 25) and optical light diffraction based on laser-induced transient grating techniques (26, 27). However, these approaches either necessitated the sample to be deposited on a substrate [affecting the surface charge dynamics and offering limited time resolution (24, 25)] or are confined to macroscopic specimens [lacking spatial resolution (26, 27)].

Beyond a solid-state physics approach, a comprehensive understanding of how photo-induced surface charges affect the bonding motifs of surface functional groups is lacking in the literature for isolated nanosystems. Direct imaging of ultrafast surface charge dynamics on isolated NPs after laser irradiation is crucial for achieving such a goal. Unlike plasmonic metal NPs, which incur substantial energy losses and heat generation when interacting with light, dielectric NPs provide an energy-efficient alternative (28). Here, we present an approach to visualize surface charge dynamics on the surface of individual and isolated dielectric silicon dioxide (SiO_2) NPs subjected to infrared (IR) irradiation in real time. Using time-resolved reaction nanoscopy (29), we uncover the ultrafast generation and redistribution of surface charges and demonstrate their influence on the terminal functional groups at the vacuum-NP interface.

[1]Faculty of Physics, Ludwig-Maximilians-Universität Munich, D-85748 Garching, Germany. [2]Max Planck Institute of Quantum Optics, D-85748 Garching, Germany. [3]State Key Laboratory of Precision Spectroscopy, East China Normal University, Shanghai 200241, China. [4]Stanford PULSE Institute, SLAC National Accelerator Laboratory, Menlo Park, CA 94025, USA. [5]Nanoinstitute Munich, Faculty of Physics, Ludwig-Maximilians-Universität Munich, D-80539 Munich, Germany. [6]Collaboratory for Advanced Computing and Simulations, University of Southern California, Los Angeles, CA 90089, USA. [7]Department of Physics, Kumamoto University, Kumamoto 860-0862, Japan. [8]Department of Physics, Escuela Politecnica Nacional, Quito 170525, Ecuador. [9]Department of Physics, Imperial College London, London SW7 2AZ, UK. [10]School of Physics and Astronomy, Monash University, Clayton, Victoria 3800, Australia. [11]Applied Physics Department, Stanford University, Stanford, CA 94305, USA.
*Corresponding author. Email: ritika.dagar@physik.uni-muenchen.de (R.D.); wbzhang@lps.ecnu.edu.cn (W.Z.); mfkling@slac.stanford.edu (M.F.K.)
†These authors contributed equally to this work.
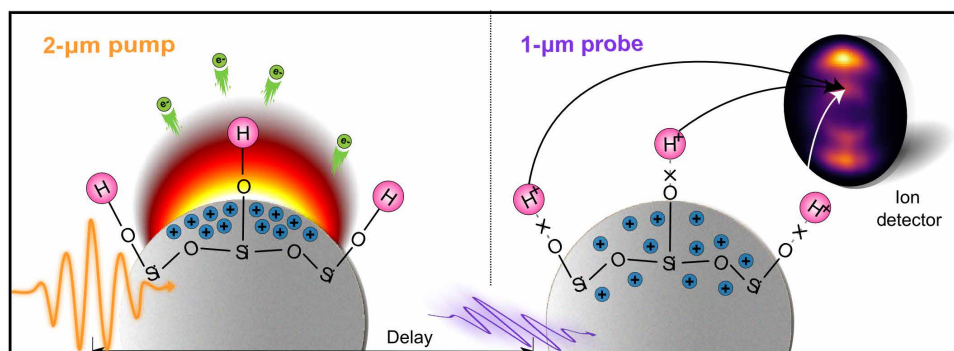
RESULTS

Experimental results

We used the reaction nanoscopy technique in conjunction with a two-color pump-probe scheme (see Fig. 1). Using three-dimensional ion momentum spectroscopy, the reaction nanoscope enables the visualization of near-field–induced reaction yield distributions on isolated NP surfaces (30, 31). The technique relies on a point-projection approach that maps ion momentum distributions to real-space emission from the nanosurface. In the experiments described here, as depicted in Fig. 1, an IR pump pulse was used to ionize the NP, resulting in the release of electrons and the generation of positive surface charges on individual SiO_2 NPs. Following a delay, a probe pulse induces the dissociation of ions from the terminal groups, such as physisorbed and chemisorbed solvent (ethanol) molecules ($Si-O-CH_2CH_3$) as well as O-H groups from silanols on the particle surface (31). The emitted ion fragments act as sensitive markers of the local chemical reaction landscape, where the pump pulse–induced surface charges play a dominant role in influencing bond dissociation. Here, we used protons to probe the surface charge dynamics owing to their ubiquity among all emitting ions.

The experimental framework involved generating an aerosolized beam of spherical dielectric SiO_2 NPs using an atomizer and aerodynamic lens system. The aerodynamic focusing system allows for the investigation of single NPs and ensures a fresh sample for each laser shot. The pump consisted of laser pulse centered around the wavelength of 2 μm, with a pulse duration of ~35 fs at an intensity of ~2 × 10^{13} W/cm². The second harmonic of the pump pulse at 1 μm, with a pulse duration of ~40 fs and intensity ~3.8 × 10^{12} W/cm², polarized perpendicularly to the pump pulse, was used as the probe. The orthogonal selection of the polarization direction for pump-probe pulses was vital for distinguishing the unique interaction of individual pulses with the NP surface leading to distinct optical and chemical hotspots on the NP surface for each pulse. We used moderate laser intensities to suppress plasma formation (32) and particle expansion (15, 16) upon irradiation. The distinct abundance of released electrons, detected with a channeltron detector was used to differentiate NP events from background gas. A time- and position-sensitive detector reconstructed the three-dimensional (3D) ion momentum distribution. More experimental details can be found in the Supplementary Materials.

Figure 2 represents the measured proton momentum and kinetic energy (KE) distributions for 300-nm SiO_2 nanospheres. Figure 2 (A and B) shows dipolar momentum distributions observed from the pump and probe pulses separately, i.e., 2-μm pump and 1-μm probe pulses along their polarization in the y and z directions (defined in the laboratory frame), respectively. Such features agree with previous experimental results (29–31, 33) in which the ion momenta distribution closely follows the laser polarization–sensitive local field enhancement around the NP. In our work, we identified an additional feature at lower momentum, contained by the dashed box (see Fig. 2C) that depicts the time-integrated proton momentum distribution in the shared polarization plane of both pulses, i.e., $p_x = 0$ plane. Figure 2D displays the proton KE spectrum as a function of the pump-probe delay. The spectrum can be separated into two parts: proton energies above and below 20 eV. The high-energy band (~28 eV) is delay independent, which mainly originates from individual pump or probe pulses. However, the energy region below 20 eV shows a clear time dependence where the proton KE decreases with increasing pump-probe delay. Starting from the same energy region as the single pulse–induced high-energy band (>20 eV in Fig. 2D), the proton KE decreases as a function of time delay, to an asymptotic energy of ~2.3 eV within approximately 300 ps.

Focusing our analysis on the low-KE region of the proton momentum distribution, corresponding to the inner momentum ring in Fig. 2C, one observes that protons are emitted along the polarization direction of the pump pulse. This is observed even though the probe is perpendicularly polarized to the pump and is primarily responsible for triggering proton emission. We observed consistent results for the negative delays in which the 1-μm pulse serves as the pump (see fig. S3). Our investigation further revealed that a single exponential curve proved inadequate in accurately representing the time-dependent decay of KE observed in the experiments. As a result, we used a biexponential model to better capture and model the observed decay trace. Two distinct time constants were derived from the fitting, a faster process occurring around the timescale of ~10 ps, while the slower process exhibits decay over a

Fig. 1. The pump-probe scheme for probing surface charge dynamics on SiO₂ NPs. Surface charges are generated on a silica NP by an infrared (IR) pump pulse, which ionizes the NP through intense near-fields, releasing electrons and resulting in the creation of positive surface charges (illustrated by blue plus signs), as depicted on the left. The presence of the surface charge weakens the terminal O-H bonds at the interface by delocalizing the electron density under the influence of the strong positive potential on the surface. The probe pulse, polarized perpendicularly to the pump pulse, dissociates the weakened bonds, resulting in the emission of protons (H⁺ ions) in the polarization direction of the pump pulse. The protons' momentum distribution is used to spatially map the proton emission from the surface and, consequently, the distribution of surface charges as a function of the pump-probe delay.
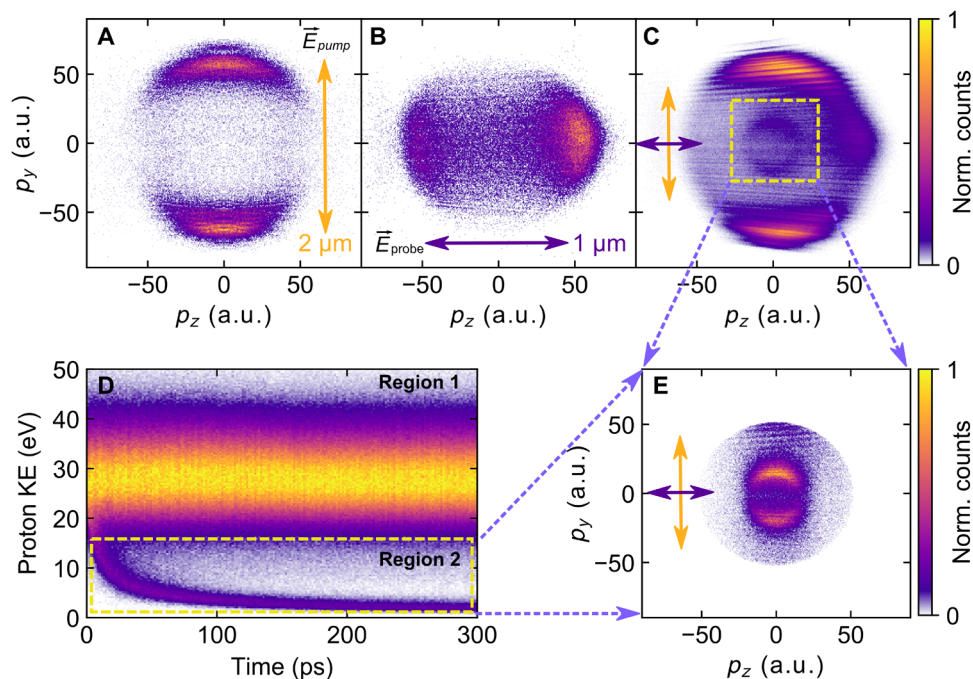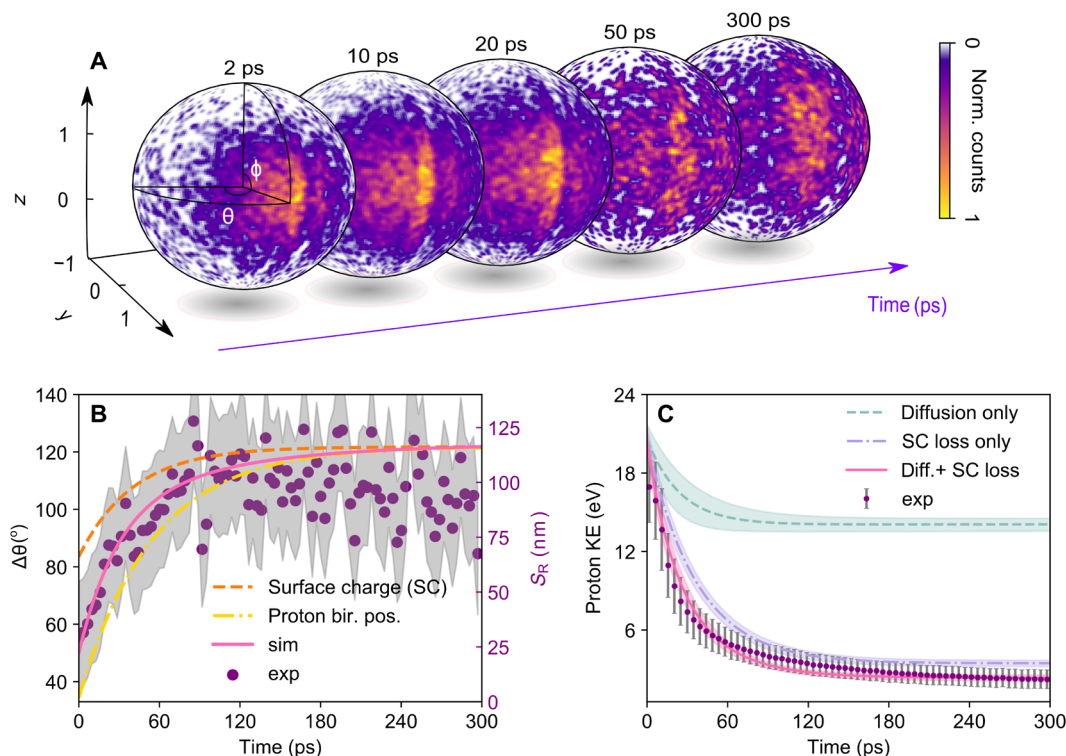
Fig. 2. Proton momentum and KE distributions. Proton momentum distribution in the laser polarization plane measured by individual (**A**) *y*-polarized 2-µm pulse and (**B**) *z*-polarized 1-µm pulse. (**C**) The time-integrated proton momentum distribution ($p_x = 0$ plane) when both 2- and 1-µm pulses are introduced, where the 2-µm pulse serves as the pump and 1-µm pulse serves as the probe. An additional feature at lower momentum is identified within the yellow-dashed square, distinct from the individual contributions of 2- and 1-µm pulses (A and B). (**D**) Proton KE spectrum measured as a function of time delay between 2- and 1-µm pulses (2-µm pulse preceding 1-µm pulse). (**E**) The proton momentum distribution associated with the time-dependent KE decay signal in region 2 of (D) coincides with the inner ring structure marked by the dashed square in (C).

longer duration with a time constant of roughly 70 ps. The biexponential KE decay trace feature is also observed for NPs with sizes of 200 nm and 600 nm, where the fitting results show that the timescales of the fast and slow process are generally shorter for smaller NPs. This can be attributed to the reduced surface areas of smaller NPs, highlighting a notable influence of particle size on the surface charge dynamics (cf. fig. S4, see the Supplementary Materials for more details).

The observed polarization-sensitive proton momentum distribution in the pump-probe experiment implies that the delay-dependent proton emission involves a two-step process. At first, positive surface charges are generated by the initial pump pulse whose distribution aligns with the laser's polarization-sensitive near-fields. The interaction between surface charges created by the pump pulse and the highly electronegative surface oxygen atoms of the NPs prompts an induced polarization within the surface bonds of the NPs. This induced polarization leads to a redistribution of the electron density within the surface bonds and leads to bond weakening, further corroborated by our quantum dynamical simulations as discussed later. Since the surface molecular bonding has been weakened by the adjacent local surface charges, in the second step, the later-arriving, perpendicularly polarized probe pulse can more readily yield surface molecular dissociation with the generation of protons closely correlating with the surface charge distribution. In the course of dissociation, the surface charges attract electron density away from the dissociating surface groups, leading to a reduction in the coulombic potential across the NP surface. Therefore, the coulomb potential experienced by the protons is reduced, leading to a slowdown of the

KE decay after a few tens of picoseconds. A similar feature is observed with H_2^+ emission (see fig. S6).

As shown in Fig. 3, the proton momentum distributions in the low-KE region also exhibit an angular broadening. Figure 3A provides a visual representation of the 3D (ϕ, θ, and r) angular proton momentum distribution at different time intervals, capturing the evolving pattern of the time-dependent momentum distribution of the protons exhibiting KE-decay. The variation in the distribution of θ, i.e., $\Delta\theta$, to time, is depicted in Fig. 3B. The results elucidate an exponential redistribution of the surface charges accompanied by a wider distribution of proton birth positions and consequently proton momentum distribution. The proton angular broadening occurs more rapidly during the initial short-time delays (less than 30 ps) and slows down at later time delays (beyond 50 ps), eventually reaching a plateau over 100 ps. The $\Delta\theta$ increases swiftly within the first 30 ps, increasing roughly from 50° to around 80°, accompanied by a proportional reduction in proton KE (~24 to ~7.7 eV). The observed proton KE decreasing and angular broadening over time can be attributed to two factors. First, as the initially localized surface charge distribution spreads out, the emitted protons are expected to possess lower final proton KE due to the diminishing coulomb force associated with the reduced surface charge density. The decrease in the width of the proton KE distribution can be attributed to the reduced gradient of the local surface charge density distribution over time. Second, since the directionality of proton emission is closely correlated with the surface charge distribution, a broader angular distribution of protons is anticipated when the charge distribution itself broadens.

Fig. 3. Angular proton momentum distribution. (**A**) Snapshots of the 3D angular proton momentum distribution at various time delays, reflecting changes in the spread of the surface charge distribution over time. The 3D momentum distributions of protons (ϕ, θ, and r) are integrated radially and projected onto a unit sphere as a 2D density map (ϕ and θ). The sphere coordinates are defined by elevation (ϕ) and azimuthal (θ) angles within specific intervals, where θ spans $[-\pi, \pi]$ relative to the x axis (propagation direction), and ϕ spans ($[-\pi/2, \pi/2]$ in relation to the y-z plane (pump polarization, time of flight). The color scale represents the proton count within each angle. (**B**) The variation in the delay-dependent full-width half maximum values of the angular distribution θ in (A), represented by $\Delta\theta$, as extracted from the Gaussian fits for the time-sliced theta distributions. The gray shaded area depicts the standard errors from the fittings. The angular broadening of the simulated angular distributions of surface charges (orange dashed curve), proton birth position (yellow dashed-dot curve), and proton momentum distributions (pink solid curve) are also shown. (**C**) Mean proton KE values derived from the simulations with different set parameters as a function of time, along with the experimental values. The dashed curve shows proton KE decay over time in the case of surface charge diffusion only and charge loss only denoted by the dash-dotted line, and the solid line combines both cases. Purple dots with gray error bars indicate experimentally measured mean proton KE values with associated standard deviations.

By translating the proton emission angle width to the spatial position of surface charges using the formula, $S_R(\theta) = \pi\{[\Delta\theta(t) - \Delta\theta(t = 0)]/(2 \times 360°)\}d$, where d is the diameter of the NP, one can obtain the time-dependent relative change in the position of charges to their birth position on the NP surfaces. The right, purple axis in Fig. 3B denotes the relative change in proton birth positions, S_R, spatially on the 300-nm SiO_2 nanosphere. The calculation is based on the near one-to-one mapping between the initial proton birth position and final proton momentum (*31*). We trace the relative spatial movement of surface charges through the dissociation of protons caused by the presence of these surface charges. Therefore, our analysis, on one hand, uncovers how the surface charge redistribution dynamics affect the proton birth position and their final momentum and on the other hand, underscores the crucial impact of the surface charge distribution on proton emission via surface bond weakening. This methodology enables us to track the spatiotemporal evolution of surface charge density with nanoscopic spatial resolution and femtosecond-temporal resolution.

Theoretical results
We used two different simulation frameworks to understand the observed charge dynamics and the molecular bond weakening on the

surface of SiO_2 NPs (see more details in the Supplementary Materials). We first performed the diffusion model–based classical trajectory Monte Carlo (d-CTMC) simulations to understand the process of surface charge redistribution. The nonadiabatic quantum molecular dynamics (NAQMD) simulations (*34*, *35*) demonstrate the role of the local surface charges created by the pump pulse in weakening of bonds of adjacent surface molecular groups.

To evaluate the role of surface charge diffusion and loss of charge on the proton KE dynamics, we used the d-CTMC simulations. In this model, local positive surface charge distribution was generated on a defined-size spherical particle by quasi-static ionization, leaving point-like positively charged ions (*30*, *31*, *33*). These charges' initial distribution correlates with enhanced near-fields induced by the pump laser. A Gaussian random walk simulates the charge redistribution based on the diffusion process. The protons are propagated in the electrostatic field of redistributed charges in each time step. We then routinely calculated the final proton momentum spectrum as a function of time. Our study explores the diffusion-based charge relaxation coupled with charge loss on proton dynamics. As shown in Fig. 3 (B and C), the simulation results qualitatively match the experimental observations of broadened proton angular momentum distributions and time-resolved proton KE decay features.

Simulations were also performed for 200- and 600-nm particles (see fig. S4), where the simulation results practically match the overall trends of the experimentally measured KE decay structure, indicating the predictive capability of our d-CTMC model across different particle sizes. The d-CTMC simulations yield notable key parameters, a diffusion coefficient of approximately 1.35 cm²/s, and the charge decay constant, whose value is approximated to be around 40 ns, taking into account some amount of residual charge.

In the d-CTMC simulations, it was postulated that the likelihood of proton dissociation from silanols at the NP surface is influenced by the presence of surface charges generated by the pump pulse, which, in turn, eases the weakening of these bonds and eventually leads to dissociation during their stretching by the probe pulse. To verify and quantify this, we used the NAQMD simulations on an amorphous silica surface terminated with Si-OH and Si-OH₂ groups in the presence of excited holes from the valence band maximum (VBM). Figure 4A shows the simulation slab replicated, the two white lines representing the periodic boundary condition. We examined the bond dynamics for the O-H bond on the surface for which the hole wave function had the highest Mulliken population. Figure 4B shows the bond dynamics for the O-H bond with and without the presence of any holes. The excitation of a single hole from the VBM weakens the bond resulting in longer stretching length and lower stretching frequency. If the VBM becomes doubly unoccupied the O-H bond quickly breaks. The initial pump pulse is anticipated to generate many holes that can quickly dissociate O-H bonds and leave the NP. The remaining holes that have not led to dissociation still weaken the O-H bond, which can be later broken by the probe pulse during the stretching of the bonds. This underscores the crucial role of local surface charge in affecting surface adsorbate bonding by inducing bond weakening.

DISCUSSION

Our d-CTMC simulations indicate that the angular broadening observed in the proton momentum distribution (see Fig. 3B) primarily stems from diffusion, as it spreads initially localized surface charges over time due to its stochastic nature. However, simulations using just diffusion toward a homogeneous distribution were unable to accurately model the entire proton KE decay profile even though they were able to reproduce the initial rapid decline. Implementing a charge loss mechanism driven by proton detachment markedly enhanced the agreement between our simulations and the experimental data. Protons emitted through this mechanism will achieve a reduced final KE owing to the diminished coulomb force resulting from the lower number and increased separation of the surface charges as a consequence of the considerable effect of electrostatic interactions from the charged NP surface. Examining the energy loss in protons allows us to probe the local and overall surface charge density on the NP surface. The initial ion momentum from molecular dissociation is considered negligible. Our study is not only able to comprehend the roles of both diffusion and charge loss in the spatiotemporal dynamics of surface charges but is able to distinguish them based on the order of magnitude of their characteristic timescales. The ability to extract and differentiate the timescales of these processes on isolated NPs permits comparison to theoretical predictions and ultimately drives a deeper understanding of NP-driven catalysis and related charge-mediated processes.

The calculated diffusion coefficient of around 1.35 cm²/s in the simulations is indicative of the unique characteristics of the strong-field ionization of the SiO₂ NPs. In comparison to a degenerate electron gas (i.e., simple metal), such a diffusion constant would be small (36), but it is quite large for typically reported photocarrier transport coefficients (37–39), and in comparison to typical photocatalytic material TiO₂, our reported diffusion constant is three orders of magnitude larger than its bulk value (40). The corresponding charge carrier mobility for our reported diffusion constant would be on the high end for those observed in heavily doped wide bandgap semiconductors (41). As the trapping field arising from the positively charged surface and free electrons created by the strong field ionization of SiO₂ NPs leads to strong charge interactions and increased charge mobility at the surface (42), our reported diffusion constant, between that of a heavily doped semiconductor and a degenerate electron gas is consistent with this scenario. The charge decay constant, approximately 40 ns, also exhibits a degree of similarity with reported values observed in analogous systems. For instance, in rutile TiO₂, the lifetimes of holes were found to exceed several hundred picoseconds (43). Development of next-generation photocatalytic materials is extremely reliant on knowledge and ability to engineer charge carrier lifetime and diffusion properties, with typically long charge migration times sought to maximize reactivity (44). The implemented pump-probe reaction nanoscopy allows the evaluation of these properties at the nanoscale.
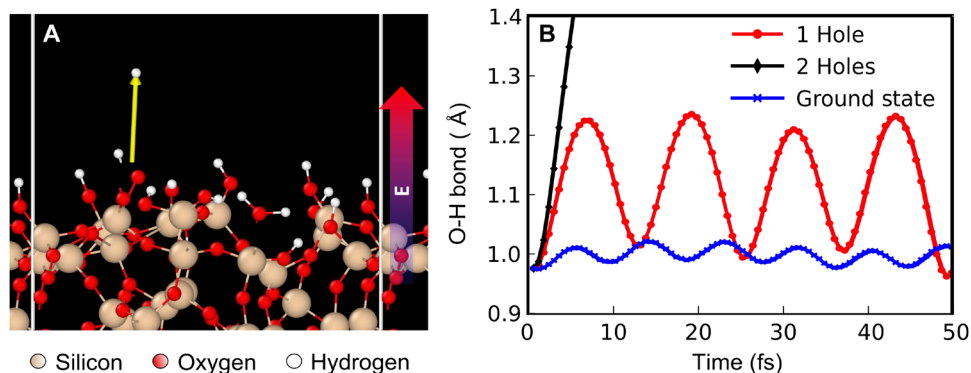
Fig. 4. Bond weakening due to the presence of surface charges. (**A**) Simulated silica slab representing a ~1-nm² chunk of silica in the presence of a strong DC field generated by the surface charges. The white lines depict the implemented periodic boundary conditions. (**B**) O-H bond dynamics with and without the presence of holes.

Our theoretical framework offers a highly intuitive interpretation of our experimental observations. We do acknowledge some limitations in our calculations, as there are additional processes, such as charge-charge interactions and surface scattering, which may influence the diffusion and charge loss process. For instance, since charge-charge interactions and surface scattering that mostly occurr within tens of picoseconds are not included in our simple model, the simulated proton KE decay traces for different particle sizes slightly deviate from the experimentally observed trends at short time delays. By taking into account these complex factors, a more quantitative and extensive knowledge of the intricate functioning of nanomaterials can be achieved. Nevertheless, our simple approach combined with the experimental findings furnishes a thorough and clear understanding of the nanoscale redistribution dynamics of surface charges on individual NPs. This framework can provide a valuable means to comprehend diverse nanomaterials and, more generally, charge-mediated processes on surfaces.

In conclusion, we demonstrated 4D visualization of surface charge dynamics on laser-irradiated dielectric silica NPs through pump-probe reaction nanoscopy. The semi-classical simulations manifested distinct timescales for the dispersion and loss of surface charges, yielding the experimentally observed biexponential decline in the kinetic energies of the dissociating protons. The NAQMD simulations revealed the strong influence of the surface charges on the bonding of surface functional groups, demonstrating the capability of charged dielectric NPs to trigger chemical reactions at the surface. Such dynamics are tracked via the probe and can be used to reconstruct charge diffusion and decay properties. In the context of silica NPs, these findings explain the peculiar catalytic reactivity previously observed in related studies (3). In a broader sense, the time-resolved experiments of charge dynamics on a single NP level can be used to investigate the role of particle material and morphology on charge carrier dynamics. Such understanding will be critical for optimizing charge-induced heterogeneous catalysis.

MATERIALS AND METHODS
Experimental setup of pump-probe reaction nanoscopy
As schematically illustrated in fig. S1A, the experimental approach was the realization of time-resolved pump-probe measurements in the reaction nanoscope, also referred to as NanoTRIMS (nano-target recoil ion momentum spectroscopy) (29–31, 33). In the experiment, a mid-IR pulse from an optical parametric chirped-pulse amplification laser system (~17 fs, 2 µm, and 100 kHz) (45) was frequency doubled in a 1.5-mm-thick lithium niobate crystal. The two colors were separated in two arms of an interferometer using a dielectric mirror to produce a 2-µm pump pulse and a 1-µm probe pulse. Two customized chirped mirrors were installed in each arm to optimize the laser pulse duration (2 µm, ~35 fs; and 1 µm, ~30 fs). The time delay between the pump and probe pulses was finely controlled by using a motorized delay stage (Physics Instruments, PI-M406.4PD). The linearly polarized pump and probe pulses were later recombined with a dielectric mirror. The collimated laser beams were tightly focused by a concave silver mirror ($f = 75$ mm) inside the NanoTRIMS vacuum chamber, where they crossed the SiO_2 NP beam. The SiO_2 NPs of uniform size (304 $\pm$ 19 nm) were synthesized through the process described in the following section. To produce the NP jet, NPs dispersed in pure ethanol with concentrations of 0.1, 0.2, and 0.5 g/liter for 200, 300, and 600 nm particle

sizes were aerosolized using a compressed gas atomizer (TSI, model 3076). The detailed method for NP synthesis and sample preparation can be found in a previous publication (31). The argon-carried NPs were dragged through a nafion-tubed membrane dryer (Perma Pure, PPMD-700-48S-1) to achieve a large removal of solvent. Afterward, the NP aerosol was introduced into the ultrahigh vacuum ($<2 \times 10^{-10}$ mbar) chamber via an aerodynamics lens system, resulting in a collimated beam of isolated NPs streaming through the vacuum.

Upon the interaction of the NPs with the focused strong laser pulses, the laser-created energetic ions and electrons ejecting from the NPs were guided by a homogenous electric field (~198 V/cm) to be detected in coincidence by two different detectors. A time- and position-sensitive detector consisting of a microchannel plate stack and delay-line detector (DLD80, RoentDek Handels GmbH) was used to measure the ion's time-of-flight and impact positions from which the reconstruction of their full 3D momentum distributions was made. The hit rates of electrons associated with each laser shot were recorded using a channeltron electron amplifier (Photonis Magnum) at the opposite side of the NanoTRIMS spectrometer. As shown in fig. S1B, a much higher channeltron signal was measured from NP-associated ionization events than that coming from background gas. The electrons and ion emission originating from molecular adsorbate ionization and dissociation events can thus be clearly distinguished.

NP synthesis
Tetraethylorthosilicate 98% (TEOS), ammonium hydroxide solution 28 to 30% (NH_4OH), and pure-grade ethanol were purchased from Sigma-Aldrich. All chemicals were used as received and Milli-grade water was used in all preparations. Monodisperse silica spheres (304 $\pm$ 19 nm) were prepared using a modified Stöber method (46). A total of 25 ml of EtOH solution containing 9.17 ml of H_2O, 2.44 ml of NH_4OH, and 1.42 ml of TEOS was quickly added and the mixture was kept for 2 hours. The resultant SiO_2 nanospheres were washed with ethanol by three centrifugation-redispersion cycles (5000 rpm, 15 min).

d-CTMC simulations
The basis of the d-CTMC simulations is similar to the static field model as used in references (29–31, 33) and is adapted to capture the time-dependent surface charge dynamics. At first, the near-field distribution around silica spheres with a given size and refractive index of 1.5, was calculated using the Mie solution numerically. The initial local surface charges are generated using the Monte-Carlo rejection sampling technique based on the Ammosov, Delone, and Krainov (ADK) (47) ionization rate as point charges on the particle surface according to the near-field–dependent ionization probability distribution for a 2-µm laser pulse. For the ADK calculations, we used the maximum peak electric field above the NP surface. The protons' birth positions for the first laser pulse were sampled according to the dissociation ionization probabilities modeled by a power law I^n, specifically using $n = 26$, ensuring consistency with the 2-µm laser wavelength used in this study, multiplied by a radial Gaussian distribution ($r_0 = 150$ nm and $\sigma_r = 30$ nm) to account for the spatial distribution of the molecules. We note that once the pump pulse has subsided, it leaves a highly positively charged NP surface. The post-laser "equilibrium phase" of the surface charge redistribution is considered to be dominated by the

diffusion of charges and charge loss. To model that, we diffused the mother ions sampled on the surface by a Gaussian random walk along the surface, also reckoning the charge loss mechanism via the exponential decay equation

$$Q(t) = Q_0 e^{-kt} + Q_{residual} \qquad (1)$$

Here, $Q(t)$ denoted the number of surface charges remaining at time t, Q_0 is the initial amount of charge, k is the charge decay constant that characterizes the number of charges decreasing over time, and $Q_{residual}$ is the residual charge that represents the remaining charge on the surface after the time window for the simulation has elapsed. The 3D random walk is governed by a diffusion coefficient, where the step size is drawn randomly from a Gaussian distribution multiplied by $\sqrt{6D\tau}$ expressing the mean displacement with a time step τ, moving in random directions. Here, D denotes the diffusion coefficient. The total number of steps is calculated by dividing the time interval by $\tau = 1$ ps (also tested for smaller steps of 500 fs leading to the same results), for each progressing time step. During each diffusion step, we enabled the sampled protons to undergo classical propagation away from the surface, influenced by the electrostatic field of the surface charges according to Newton's law to obtain the final 3D momentum spectra. We then gathered the resulting 3D momentum spectra of the protons at each step (31, 33). The diffusion coefficient, 1.35 cm^2/s, and the charge decay constant approximated as 40 ns were adjusted as fitting parameters to align the decay behavior with the experimental results. In the context of proton sampling, we postulated that the probability of proton generation is influenced by the presence of a surface charge, which facilitates bond weakening. To address the nonlinear distribution of the local charge density, and thus, proton sampling positions, we adopted an initial proton sampling region with a power-law dependence. This initial region was subsequently subjected to diffusion, reflecting the dynamics of surface charges. For the simulations, we introduced a second pulse to trigger the dissociation of weakened bonds in the presence of the high electric field–induced polarization of the NP. As a result, proton generation was found to be enhanced in regions with higher local surface charge density.

In the model, it is assumed that the protons emitted with an initial velocity of zero are propagated independently of each other and the emission dynamics are dominated by the electrostatic interactions with the positively charged NP surface. The effect of coulomb interaction from the fast escaping electrons on the final proton momenta is assumed to be negligible. In the model, the number of sampled static surface charges for the normalization of initial charge distribution ρ_{charge} was estimated to be ~$1810e$ by fitting the single–2 μm–induced proton KE distribution at an intensity of 4×10^{13} W/cm^2.

NAQMD simulations

To examine the role of charge generation on bond softening and proton dissociation in the silica nanosphere, we adopted a multiscale approach, as first-principle simulations are unable to simulate surfaces on the size of the NP. We apply a strong DC field along a silica surface to model the effect of the fields induced by the global hole density on the nanosphere similar to globally informed Hartree-potential frameworks in divide and conquer density functional theory (DFT). Thus, the simulated silica surface represents a ~1-nm^2 chunk of silica embedded in an ionized nanosphere. To obtain an order of magnitude estimate of the fields induced on a nanosphere

from a nonuniform ionized charge density, we first use a Mie field solver to obtain the near field enhancement at the nanosphere surface for a given pump pulse. From the local optical fields, we generate an ionized charge distribution using the ADK theory (47). The integrated ADK rate is used to determine the probability density of ionization for any given surface area element, and the total ionized charge density is the set as density of SiO$_2$ in crystalline silica times the ionization probability (48). Figure S2A shows the charge distribution at the surface as a function of the polar angle θ for an intensity 5×10^{13} W/cm^2. To obtain the electric field induced by the charge density, we solved Poisson's equation via a multipole expansion, and the field at the NP surface is plotted in fig. S2B. While many approximations were made to obtain this field, the goal was to inform boundary conditions for NAQMD dynamics simulations for which only an order of magnitude estimate of expected electric fields generated in the experiments is required.

NAQMD simulations were performed on a 14.32–Å–cubic length amorphous silica structure. Along the one of the cubic axes, we created a hydrogen-terminated surface and added an additional vacuum to prevent image interactions. An electric field of 0.02 atomic units (~1 V/Å) was applied using a sawtooth potential. NAQMD simulations are an ab initio molecular dynamics approach that integrates the trajectories of all atoms by computing their intermolecular forces from first principles in the framework of DFT. To approximate the exchange-correlation functional in our DFT approach, we used the Perdew-Burke-Ernzerhof version of generalized gradient approximation (49). Van der Walls corrections were used using the DFT-D scheme (50). The projected argument wave vector method was used to calculate electronic states within a plane wave basis set (51). Projector functions were generated for the Si-3s and 3p states, O-2s and 2p states, and the 1s state for hydrogen. A planewave cutoff energy of 35 Ry was used. NAQMD allows for dynamics of excited carriers to be modeled within the framework of the time-dependent DFT. Excited state transitions were modeled within the fewest switch surface hopping method (52). Dynamics were performed in the microcanonical ensemble at 300 K. The NAQMD algorithm was implemented in the QXMD quantum molecular dynamics simulation code (53). For further details of the NAQMD algorithm, we refer the readers to references (34, 35, 53).

Figure S2C shows dynamics of an O-H bond on the surface for which the hole wave functions had the highest Mulliken population. For two holes excited from the VBM, the O-H bond quickly dissociates. With one hole excited, a clear bond softening is seen in comparison to the field and hole free ground state. The decline in O-H stretching vibrational energy is illustrated in fig. S2D taken from Fourier transform of the O-H bond length dynamics. This softening can lead to breaking during the stretching of the bond by the probe pulse.

Supplementary Materials

This PDF file includes:
Supplementary Text
Figs. S1 to S6
References

REFERENCES AND NOTES

1. M. Murdoch, G. I. N. Waterhouse, M. A. Nadeem, J. B. Metson, M. A. Keane, R. F. Howe, J. Llorca, H. Idriss, The effect of gold loading and particle size on photocatalytic hydrogen production from ethanol over Au/TiO$_2$ nanoparticles. *Nat. Chem.* **3**, 489–492 (2011).

2. R. Gupta, B. Rai, Effect of size and surface charge of gold nanoparticles on their skin permeability: A molecular dynamics study. *Sci. Rep.* **7**, 45292 (2017).

3. M. S. Alghabra, R. Ali, V. Kim, M. Iqbal, P. Rosenberger, S. Mitra, R. Dagar, P. Rupp, B. Bergues, D. Mathur, M. F. Kling, A. S. Alnaser, Anomalous formation of trihydrogen cations from water on nanoparticles. *Nat. Commun.* **12**, 3839 (2021).

4. U. M. Kannana, L. Giribabub, S. N. Jammalamadaka, Demagnetization field driven charge transport in a TiO₂ based dye sensitized solar cell. *Sol. Energy* **187**, 281–289 (2019).

5. D. H. Jo, J. H. Kim, T. G. Lee, J. H. Kim, Size, surface charge, and shape determine therapeutic effects of nanoparticles on brain and retinal diseases. *Nanomedicine* **11**, 1603–1611 (2015).

6. M. J. Mitchell, M. M. Billingsley, R. M. Haley, M. E. Wechsler, N. A. Peppas, R. Langer, Engineering precision nanoparticles for drug delivery. *Nat. Rev. Drug Discov.* **20**, 101–124 (2021).

7. J. Repp, G. Meyer, F. E. Olsson, M. Persson, Controlling the charge state of individual gold adatoms. *Science* **305**, 493–495 (2004).

8. C. Y. J. Lim, M. Yilmaz, J. M. Arce-Ramos, A. D. Handoko, W. J. Teh, Y. Zheng, Z. H. J. Khoo, M. Lin, M. Isaacs, T. L. D. Tam, Y. Bai, C. K. Ng, B. S. Yeo, G. Sankar, I. P. Parkin, K. Hippalgaonkar, M. B. Sullivan, J. Zhang, Y.-F. Lim, Surface charge as activity descriptors for electrochemical CO₂ reduction to multi-carbon products on organic-functionalised Cu. *Nat. Commun.* **14**, 335 (2023).

9. J. Gallagher, Charging effects come to the surface. *Nat. Energy* **8**, 112 (2023).

10. H. Harutyunyan, F. Suchanek, R. Lemasters, J. J. Foley, Hot-carrier dynamics in catalysis. *MRS Bull.* **45**, 32–36 (2020).

11. Y. Bai, H. Huang, C. Wang, R. Long, Y. Xiong, Engineering the surface charge states of nanostructures for enhanced catalytic performance. *Mater. Chem. Front.* **1**, 1951–1964 (2017).

12. S. Linic, U. Aslam, C. Boerigter, M. Morabito, Photochemical transformations on plasmonic metal nanoparticles. *Nat. Mater.* **14**, 567–576 (2015).

13. E. Cortés, Activating plasmonic chemistry. *Science* **362**, 28–29 (2018).

14. S. Zherebtsov, T. Fennel, J. Plenge, E. Antonsson, I. Znakovskaya, A. Wirth, O. Herrwerth, F. Süßmann, C. Peltz, I. Ahmad, S. A. Trushin, V. Pervak, S. Karsch, M. J. J. Vrakking, B. Langer, C. Graf, M. I. Stockman, F. Krausz, E. Rühl, M. F. Kling, Controlled near-field enhanced electron acceleration from dielectric nanospheres with intense few-cycle laser fields. *Nat. Phys.* **7**, 656–662 (2011).

15. T. Gorkhover, S. Schorb, R. Coffee, M. Adolph, L. Foucar, D. Rupp, A. Aquila, J. D. Bozek, S. W. Epp, B. Erk, L. Gumprecht, L. Holmegaard, A. Hartmann, R. Hartmann, G. Hauser, P. Holl, A. Hömke, P. Johnsson, N. Kimmel, K.-U. Kühnel, M. Messerschmidt, C. Reich, A. Rouzée, B. Rudek, C. Schmidt, J. Schulz, H. Soltau, S. Stern, G. Weidenspointner, B. White, J. Küpper, L. Strüder, I. Schlichting, J. Ullrich, D. Rolles, A. Rudenko, T. Möller, C. Bostedt, Femtosecond and nanometre visualization of structural dynamics in superheated nanoparticles. *Nat. Photonics* **10**, 93–97 (2016).

16. C. Peltz, J. A. Powell, P. Rupp, A. Summers, T. Gorkhover, M. Gallei, I. Halfpap, E. Antonsson, B. Langer, C. Trallero-Herrero, C. Graf, D. Ray, Q. Liu, T. Osipov, M. Bucher, K. Ferguson, S. Möller, S. Zherebtsov, D. Rolles, E. Rühl, G. Coslovich, R. N. Coffee, C. Bostedt, A. Rudenko, M. F. Kling, T. Fennel, Few-femtosecond resolved imaging of laser-driven nanoplasma expansion. *New J. Phys.* **24**, 043024 (2022).

17. T. Curk, E. Luijten, Charge regulation effects in nanoparticle self-assembly. *Phys. Rev. Lett.* **126**, 138003 (2021).

18. A. Bakhshandeh, D. Frydel, A. Diehl, Y. Levin, Charge regulation of colloidal particles: Theory and simulations. *Phys. Rev. Lett.* **123**, 208004 (2019).

19. C. Xu, A. C. Wang, H. Zou, B. Zhang, C. Zhang, Y. Zi, L. Pan, P. Wang, P. Feng, Z. Lin, Z. L. Wang, Raising the working temperature of a triboelectric nanogenerator by quenching down electron thermionic emission in contact-electrification. *Adv. Mater.* **30**, e1803968 (2018).

20. S. M. Kim, Theoretical study on the oscillatory triboelectric charge density in a contact-mode triboelectric nanogenerator. *Eur. Phys. J. Plus* **133**, 535 (2018).

21. T. O. Dizdar, G. Kocausta, E. Gülcan, A new method to produce high voltage static electric load for electrostatic separation-Triboelectric charging. *Powder Technol.* **327**, 89–95 (2018).

22. Y. He, W. Xie, Y. Zhao, H. Li, S. Wang, Triboelectrostatic separation of pulverized fuel of coal power plant based on mineralogical analyses. *Int. J. Miner. Process.* **166**, 7–12 (2017).

23. R. Widenhorn, A. W. Bargioni, M. M. Blouke, A. J. Bae, E. Bodegom, Charge diffusion in the field-free region of charge-coupled devices. *Opt. Eng.* **49**, 044401 (2010).

24. X. Bai, A. Riet, S. Xu, D. J. Lacks, H. Wang, Experimental and simulation investigation of the nanoscale charge diffusion process on a dielectric surface: Effects of relative humidity. *J. Phys. Chem. C* **125**, 11677–11686 (2021).

25. Y. Zhou, Y. Liu, G. Zhu, Z. Lin, C. Pan, Q. Jing, Z. Wang, In situ quantitative study of nanoscale triboelectrification and patterning. *Nano Lett.* **13**, 2771–2776 (2013).

26. M. Kozák, F. Trojánek, P. Malá, Hot-carrier transport in diamond controlled by femtosecond laser pulses. *New J. Phys.* **17**, 053027 (2015).

27. P. Ščajev, V. Gudelis, E. Ivakin, K. Jarašiunas, Nonequilibrium carrier dynamics in bulk hpht diamond at two-photon carrier generation. *Phys. Status Solidi A* **208**, 2067–2072 (2011).

28. J. Xu, Y. Wu, P. Zhang, Y. Wu, R. A. L. Vallée, S. Wu, X. Liu, Resonant scattering manipulation of dielectric nanoparticles. *Adv. Opt. Mater.* **9**, 2100112 (2021).

29. P. Rupp, C. Burger, N. G. Kling, M. Kübel, S. Mitra, P. Rosenberger, T. Weatherby, N. Saito, J. Itatani, A. S. Alnaser, M. B. Raschke, E. Rühl, A. Schlander, M. Gallei, L. Seiffert, T. Fennel, B. Bergues, M. F. Kling, Few-cycle laser driven reaction nanoscopy on aerosolized silica nanoparticles. *Nat. Commun.* **10**, 4655 (2019).

30. P. Rosenberger, R. Dagar, W. Zhang, A. Sousa-Castillo, M. Neuhaus, E. Cortes, S. A. Maier, C. Costa-Vera, M. F. Kling, B. Bergues, Imaging elliptically polarized infrared near-fields on nanoparticles by strong-field dissociation of functional surface groups. *Eur. Phys. J. D.* **76**, 109 (2022).

31. W. Zhang, R. Dagar, P. Rosenberger, A. Sousa-Castillo, M. Neuhaus, W. Li, S. A. Khan, A. S. Alnaser, E. Cortes, S. A. Maier, C. Costa-Vera, M. F. Kling, B. Bergues, All-optical nanoscopic spatial control of molecular reaction yields on nanoparticles. *Optica* **9**, 551 (2022).

32. D. D. Hickstein, F. Dollar, J. L. Ellis, K. Schnitzenbaumer, K. E. Keister, G. Petrov, C. Ding, B. Palm, J. Gaffney, M. Foord, S. Libby, G. Dukovic, J. Jimenez, H. Kapteyn, M. Murnane, W. Xiong, Mapping nanoscale absorption of femtosecond laser pulses using plasma explosion imaging. *ACS Nano* **8**, 8810–8818 (2014).

33. P. Rosenberger, P. Rupp, R. Ali, M. S. AlGhabra, S. Sun, S. Mitra, S. Khan, R. Dagar, V. Kim, M. Iqbal, J. Schötz, Q. Liu, S. K. Sundaram, J. Kredel, M. Gallei, C. Costa-Vera, B. Bergues, A. Alnaser, M. Kling, Near-field induced reaction yields from nanoparticle clusters. *ACS Photonics* **7**, 1885–1892 (2020).

34. F. Shimojo, S. Ohmura, W. Mou, R. Kalia, A. Nakano, P. Vashishta, Large nonadiabatic quantum molecular dynamics simulations on parallel computers. *Comput. Phys. Commun.* **184**, 1–8 (2013).

35. F. Shimojo, S. Hattori, R. K. Kalia, M. Kunaseth, W. Mou, A. Nakano, K.-I. Nomura, S. Ohmura, P. Rajak, K. Shimamura, P. Vashishta, A divide-conquer-recombine algorithmic paradigm for large spatiotemporal quantum molecular dynamics simulations. *J. Chem. Phys.* **140**, 18A529 (2014).

36. V. Palenskis, Drift mobility, diffusion coefficient of randomly moving charge carriers in metals and other materials with degenerated electron gas. *World J. Condens. Matter Phys.* **03**, 73–81 (2013).

37. X. Gong, Z. Huang, R. Sabatini, C.-S. Tan, G. Bappi, G. Walters, A. Proppe, M. I. Saidaminov, O. Voznyy, S. O. Kelley, E. H. Sargent, Contactless measurements of photocarrier transport properties in perovskite single crystals. *Nat. Commun.* **10**, 1591 (2019).

38. S. D. Stranks, G. E. Eperon, G. Grancini, C. Menelaou, M. J. P. Alcocer, T. Leijtens, L. M. Herz, A. Petrozza, H. J. Snaith, Electron-hole diffusion lengths exceeding 1 micrometer in an organometal trihalide perovskite absorber. *Science* **342**, 341–344 (2013).

39. M. Kissel, L. Porz, T. Frömling, A. Nakamura, J. Rödel, M. Alexe, Enhanced photoconductivity at dislocations in SrTiO₃. *Adv. Mater.* **34**, e2203032 (2022).

40. N. A. Deskins, M. Dupuis, Electron transport via polaron hopping in bulk TiO₂: A density functional theory characterization. *Phys. Rev. B* **75**, 195212 (2007).

41. H. J. Kim, U. Kim, Kim, T. H. Kim, H. S. Mun, B.-G. Jeon, K. T. Hong, W.-J. Lee, C. Ju, K. H. Kim, K. Char, High mobility in a stable transparent perovskite oxide. *Appl. Phys. Express* **5**, 061102 (2012).

42. L. Seiffert, P. Henning, P. Rupp, S. Zherebtsov, P. Hommelhoff, M. Kling, T. Fennel, Trapping field assisted backscattering in strong-field photoemission from dielectric nanospheres. *J. Mod. Opt.* **64**, 1096–1103 (2017).

43. Q. Shen, K. Katayama, T. Sawada, M. Yamaguchi, Y. Kumagai, T. Toyoda, Photoexcited hole dynamics in TiO₂ nanocrystalline films characterized using a lens-free heterodyne detection transient grating technique. *Chem. Phys. Lett.* **419**, 464–468 (2006).

44. Q. Wang, K. Domen, Particulate photocatalysts for light-driven water splitting: Mechanisms, challenges, and design strategies. *Chem. Rev.* **120**, 919–985 (2020).

45. M. Neuhaus, H. Fuest, M. Seeger, J. Schötz, M. Trubetskov, P. Russbueldt, H. Hoffmann, E. Riedle, Z. Major, V. Pervak, M. Kling, P. Wnuk, 10 W CEP-stable few-cycle source at 2 µm with 100 kHz repetition rate. *Opt. Express* **26**, 16074–16085 (2018).

46. W. Stöber, A. Fink, E. Bohn, Controlled growth of monodisperse silica spheres in the micron size range. *J. Colloid Interface Sci.* **26**, 62–69 (1968).

47. M. V. Ammosov, N. B. Delone, and V. P. Krainov, Tunnel ionization of complex atoms and of atomic ions in an alternating electromagnetic field, Sov. Phys. *JETP,* **64**, 1191–1194 (1986).

48. L. Seiffert, S. Zherebtsov, M. F. Kling, T. Fennel, Strong-field physics with nanospheres. *Adv. Phys. X* **7**, 2010595 (2022).

49. J. P. Perdew, K. Burke, M. Ernzerhof, Generalized gradient approximation made simple. *Phys. Rev. Lett.* **77**, 3865–3868 (1996).

50. S. Grimme, J. Antony, S. Ehrlich, H. Krieg, A consistent and accurate ab initio parametrization of density functional dispersion correction (DFT-D) for the 94 elements H-Pu. *J. Chem. Phys.* **132**, 154104 (2010).

51. P. E. Blöchl, Projector augmented-wave method. *Phys. Rev. B* **50**, 17953–17979 (1994).

52. J. C. Tully, Molecular dynamics with electronic transitions. *J. Chem. Phys.* **93**, 1061–1071 (1990).

53. F. Shimojo, S. Fukushima, H. Kumazoe, M. Misawa, S. Ohmura, P. Rajak, K. Shimamura, L. Oftelie, S. Tiwari, R. Kalia, A. Nakano, P. Vashishta, QXMD: An open-source program for nonadiabatic quantum molecular dynamics. *SoftwareX* **10**, 100307 (2019).

54. F. Süßmann, L. Seiffert, S. Zherebtsov, V. Mondes, J. Stierle, M. Arbeiter, J. Plenge, P. Rupp, C. Peltz, A. Kessel, S. A. Trushin, B. Ahn, D. Kim, C. Graf, E. Rühl, M. F. Kling, T. Fennel, Field propagation-induced directionality of carrier-envelope phase-controlled photoemission from nanospheres. *Nat. Commun.* **92**, 5645–5649 (2015).

55. N. Ekanayake, T. Severt, M. Nairat, N. P. Weingartz, B. M. Farris, B. Kaderiya, P. Feizollah, B. Jochim, F. Ziaee, K. Borne, P. K. Raju, K. D. Carnes, D. Rolles, A. Rudenko, B. G. Levine, J. E. Jackson, I. Ben-Itzhak, M. Dantus, H_2 roaming chemistry and the formation of H_3^+ from organic molecules in strong laser fields. *Nat. Commun.* **9**, 5186 (2018).